Journal of Environmental Chemical Engineering 10 (2022) 107013

Contents lists available at ScienceDirect

Journal of Environmental Chemical Engineering

journal homepage: www.elsevier.com/locate/jece

Assessment of an integrated adsorption-regenerative catalytic oxidation process for the harnessing of lean methane emissions

Ukrit Chaemwinyoo [a,b], Pablo Marín [a], Claudia Fernández Martín [b,c], Fernando V. Díez [a], Salvador Ordóñez [a,*]

[a] Catalysis, Reactors and Control Research Group (CRC), Dep. of Chemical and Environmental Engineering, University of Oviedo, Facultad de Química, Julián Clavería 8, 33006 Oviedo, Spain

[b] Materials and Chemical Engineering Group, University of Aberdeen, School of Engineering, Fraser Noble Building, King's College, Aberdeen AB24 3UE, Scotland, UK

[c] Centre for Energy Transition, University of Aberdeen, United Kingdom

ARTICLE INFO

Keywords:
Emission treatment
Adsorption dynamics
Periodic operation
Fixed-bed reactor
Process integration

ABSTRACT

Lean methane emissions constitute an important environmental problem due to the high global warming potential of methane compared to carbon dioxide. Typical emissions (e.g., coal mines, landfills, treatment plants, etc.) have high gas flow rate and low concentration, making its harnessing a challenging task. For this reason, an integrated adsorption/desorption and regenerative catalytic oxidation process has been proposed and designed for the treatment of an emission of 4.5 Nm^3/s containing 0.20 vol% methane. To accomplish this task, methane adsorption/desorption operation has been firstly studied experimentally in a bench-scale fixed bed (adsorbent bed of 0.145 m length and 0.060 m diameter) loaded with 3 mm pellets of an activated carbon adsorbent. The information gathered on the equilibrium and kinetics, at different methane concentrations (0.20–0.50 vol%) and space velocities (WHSV 3.0–15 mol/kg h), has been used to fit a dynamic model. Then, a regenerative catalytic oxidizer has been designed and its performance studied by means of simulations. Special attention has been paid to assessing the influence of the integration of the regenerative catalytic oxidizer with the adsorption/desorption step.

Subscripts and superscripts

*	Saturation conditions.
0	Feed or inlet conditions (z = 0).
ads	Adsorption.
b	Bed.
cy	Cycle.
des	Desorption.
e	Effective.
G	Gas.
ini	Initial conditions (t = 0).
p	Particle.
S	Solid.
W	Wall.

Acronyms.

GHSV	Gas-hourly space velocity (h^{-1}).
GWP	Global warming potential.
LDF	Linear driving force.
RCO	Regenerative catalytic oxidation.
TSA	Temperature swing adsorption.
WHSV	Weight-hourly space velocity (mol/kg h).

1. Introduction

Global warming, caused by the anthropogenic emissions of greenhouse gases (carbon dioxide, methane, etc.), is one of the most important environmental concerns of the last decades. The efforts of the Governments to decrease greenhouse gas emissions have been focused in two strategies: increase of efficiency and replacement of energy sources by carbon-neutral ones (e.g., renewable sources such as wind, solar, hydropower or biomass). The increase of efficiency in industry has led to the development of new sustainable technologies and the improvement of the existing ones, in which process intensification has played an important role. Heat transfer and recuperative systems have become an important tool to recover energy from effluent streams and transfer it upstream of the process. By implementation of these intensification measures, energy consumption at industrial scale can be reduced and, hence, the emission of greenhouse gases [12,3,41,9].

Regenerative oxidizers are typically used to recover energy from

* Corresponding author.
E-mail address: sordonez@uniovi.es (S. Ordóñez).

https://doi.org/10.1016/j.jece.2021.107013
Received 7 October 2021; Received in revised form 9 December 2021; Accepted 12 December 2021
Available online 16 December 2021

Nomenclature

a	Specific surface (m^2/m^3)
c_i	Gas-phase methane concentration (mol/m^3)
C_P	Heat capacity (J/kg K)
D	Bed diameter (m)
D_{ie}	Effective axial mass dispersion coefficient (m^2/s)
D_{Pi}	Pore diffusion coefficient (m^2/s)
d_p	Particle diameter (m)
D_s	Surface diffusion coefficient (m^2/s)
F_0	Flow rate (mol/s)
k	Thermal conductivity (W/m K)
k_f	Gas-film mass transfer coefficient (m/s)
K_{int}	Intraparticle mass transfer coefficient (s^{-1})
K_{Li}	Overall mass transfer coefficient of the LDF model (s^{-1})
k_w	Kinetic constant (mol/kg s Pa)
h	Heat transfer coefficient (W/m^2 K)
L	Bed length (m)
N_{SW}	Number of switches of the flow direction (-)
p_i	Partial pressure (kPa)
q_i	Particle-average adsorbed methane concentration (mol/kg)
r_i	Rate of methane reaction or adsorption (mol/kg s)
R	Ideal gas constant (8.314 J/mol K)
t	Time (s)
t_{sw}	Switching time (s)
T	Temperature (K)
u	Superficial velocity (m)
y_{i0}	Methane mole fraction (-)
z	Bed axial coordinate (m)

Greek letters

ΔH_i	Heat of adsorption/reaction (kJ/mol)
Λ	Adsorption stoichiometry parameter, $\rho_b q_{i0}/\epsilon_b c_{i0}$ ($-$)
ϵ_b	Bed porosity(-)
η	Internal effectiveness factor
θ	Stoichiometric time, $\left(q^*_{i0}/y_{i0}\right)_{ads}/(F_0/W)_{des}$(s)
ρ	Density (kg/m^3)

effluent gas streams, like in the iron and steel, lime or glass industries, and in the abatement of gaseous emissions (e.g. volatile organic compounds). The working principle is based on the use of a solid material to store the energy of an effluent stream as sensible heat. Then, this energy is released for the heating of an influent stream. The device operates according to alternative cycles of heat storage and release. For the case of gaseous emission abatement, the oxidizer is made of, at least, two regenerative beds and a combustion chamber placed in-between [2,25,46]. First, one of the beds is used to pre-heat the feed above the ignition temperature. Then, the oxidation takes place in the combustion chamber, releasing heat and further increasing the effluent temperature. Finally, the other bed is used to store the energy of the combustion gases, in order to restore the heat drained in the pre-heating (in the previous cycle of operation). At the end of cycle, the gas flow direction is reversed and the roles of the two beds are switched. For this reason, this device is also called reverse flow reactor [26,46]. The use of a catalyst placed in the combustion chamber can decrease the ignition temperature considerably and, hence, improve the thermal efficiency of the process.

There are many methane streams of low concentration or diluted in air that can neither be injected in the natural gas network nor harnessed using traditional methods (e.g., steam reforming). Uncontrolled methane emissions are a great environmental problem, due to the high global warming potential (GWP) of methane (i.e., 1 kg of methane produces a radiative forcing over a period of 100 years equivalent to 28 kg of carbon dioxide) [31]. These emissions include those associated to the energy and mining industry, such as, ventilation air and coal bed methane in coal mines or fugitive emissions in the natural gas supply and distributing system, but also to the waste industry, such as, the biogas generated in landfills or in waste water treatment systems [16].

The use of regenerative oxidizers for the abatement of methane emissions has been proposed [15,26]. Thus, the combustion of methane (GWP = 28) to carbon dioxide (GWP = 1) prior releasing to the atmosphere reduces the net environmental impact, due to the reduction in GWP [26]. However, a minimum sustainable concentration of methane is needed to achieve an autothermal operation of the oxidizer. At autothermal conditions, the energy released by the oxidation is equal or higher than the energy lost, i.e., the energy of the effluent. Otherwise, external fuel would be required to maintain a stable operation, which is not desired from the environmental (an economical) point of view. A minimum of 0.20–0.30% methane is required in the feed for autothermal operation of regenerative catalytic oxidizers [26,28]. For lower concentrations, a concentration technique is required to increase methane content.

In the last years, the research efforts towards the enrichment of methane in lean streams have intensified. The separation of methane and nitrogen mixtures is very challenging because the physicochemical properties of these molecules are similar. Methane enrichment can be accomplished by different technologies: cryogenic separation, adsorption, membranes, etc. For large-scale processing of natural gas (with more than 50 vol% methane), cryogenic distillation is the most widely used technology for nitrogen removal. However, for low-grade methane emissions (with less than 50 vol% methane), an energy-effective and cost-effective technology, like adsorption, is a better alternative, given the energy requirements of cryogenic separation [33,37]. Membrane separation can also be an alternative technology for the medium concentration range [4,27].

Different adsorbent materials have been proposed and tested for methane/nitrogen separation [6,29]. On the one hand, many traditional porous adsorbents, such as, activated carbons [22,42], molecular sieves [45] or zeolites [17,19,29] have been investigated [30]. Activated carbons have been used for the adsorption of hydrocarbons for decades. However, for the case of methane, the adsorption capacity is low and the selectivity limited (between 3 and 4). Hybrid materials like zeolite/-carbon monoliths have also been investigated [23]. On the other hand, novel tailored materials with improved capacity and selectivity, like metal organic frameworks (MOFs), have been developed recently [17,38]. For example, $Ni_3(HCOO)_6$ exhibits an equilibrium selectivity of 6–7 [11,35]. However, these materials are expensive and some of them can present stability problems at some conditions (e.g. high temperature, water presence, etc.) [33].

The studies regarding practical applications of adsorption/desorption processes for lean methane emissions or feedstocks are scarce. Qian et al. [33,34] proposed an improved pressure swing adsorption process to produce high purity methane. Li et al. [20,21] considered the enrichment of coal bed methane using a novel pressure swing adsorption with special care for avoiding the occurrence of explosive methane/oxygen mixtures. Yang et al. [44] conducted tests in a pilot scale unit for the concentration of ventilation air methane. Hu et al. [13,14] applied vacuum swing adsorption to the concentration of low grade methane emissions. Ursueguía et al. [39] proposed the use of temperature swing adsorption to concentrate methane emissions before the combustion in a lean turbine.

The present work addresses the harnessing of lean methane emissions by means of the integration of an adsorption/desorption concentration step with a regenerative catalytic oxidizer. The aim of the adsorption/desorption process is to concentrate methane above the

minimum amount required for the autothermal operation of the regenerative catalytic oxidizer. First, the adsorption/desorption process is studied experimentally using a fixed-bed loaded with commercial activated carbon pellets. The adsorption equilibrium and kinetics are modelled by fitting to the experimental curves obtained by the step response method. Then, methane desorption dynamics is studied experimentally and used to assess the integration with the regenerative oxidizer. Finally, the performance of a scaled-up integrated regenerative catalytic oxidizer is studied by means of simulations.

2. Materials and methods

2.1. Adsorbent

The activated carbon NORIT GF-40 has been selected as adsorbent, due to its low cost and widespread use as adsorbent for volatile organic compounds. This adsorbent is microporous with a high surface area of 871 m^2/g, pore volume of 0.44 cm^3/g and average pore size 1.7 nm (obtained by nitrogen adsorption at 77 K, see Fig. 1).

2.2. Experimental device

The experimental device consisted of a stainless-steel tube of 60 mm internal diameter and 500 mm length. The tube was loaded with 0.177 kg of adsorbent as 3 mm diameter cylindrical pellets; the height of this bed was 145 mm. Two beds of glass spheres (3 mm) were placed above and below the adsorbent bed. These beds helped to distribute the gas feed uniformly over the cross-sectional area. The tube was surrounded by a temperature-controlled electric furnace. Temperature was measured on the tube wall and at the gas inlet and outlet.

The gas feed was obtained by mixing in adequate proportions 2.50 vol% methane in air, supplied in cylinders (AIR LIQUIDE), and air obtained from a compressor (INGERSOLL-RAND); a cryogenic condenser was used to remove water from the air. The gas flow rates of methane mixture and air were set using mass flow controllers (BRONKHORST). When needed, an external spiral heater was used to heat the feed before the adsorption unit. All the experiments were done at atmospheric pressure (100 kPa).

Methane concentration of the inlet and outlet streams was measured using an infrared (IR) spectrometer (ABB-URAS 14). This device provided a measurement every 1 s with very short delay, so it is adequate to study the adsorption/desorption dynamics by the step-response method. Break curves of adsorption tests were obtained by feeding gas of a given methane concentration in air to a bed containing clean adsorbent. Desorption tests started with the adsorbent completely saturated, and air was fed as sweep gas. For each gas flow rate tested, the dead time of the system (mass flow controllers, piping, and analyser) was determined experimentally following the step-response method, with the adsorbent replaced by glass spheres. The corresponding dead time was subtracted from the time-concentration break curves to quantify the dynamics due to the adsorbent.

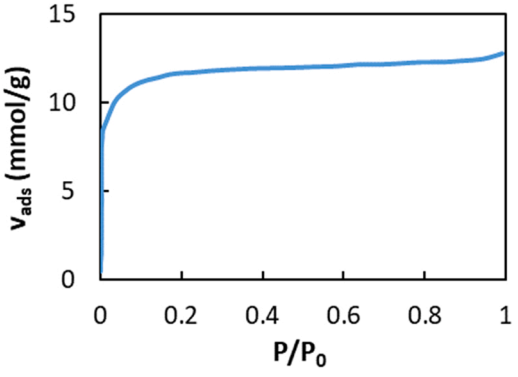

Fig. 1. Adsorption isotherm of nitrogen at 77 K on activated carbon NORIT GF-40.

2.3. Modelling of the adsorption/desorption process

The behaviour of the adsorption and desorption processes in the fixed bed has been modelled using a 1D heterogeneous dynamic model. This model is based on mass and energy conservation equations applied separately to the gas and solid phases as shown in Table 1 [26].

Mass transfer rate of methane from the gas phase to the adsorbent surface has been accounted for using the linear driving force (LDF) model [10]:

$$-r_i = \frac{dq_i}{dt} = K_{Li}\left(q_i^* - q_i\right) \quad (1)$$

Where q_i is the particle-average adsorbed methane concentration, q_i^* is the saturation concentration (i.e., equilibrium for the corresponding local gas partial pressure p_i) and K_{Li} is the overall mass transfer coefficient of the LDF model. This differential equation must be solved together with the equations of Table 1 to calculate the profiles of q_i.

The axial mass (D_{ie}) and heat (k_{Ge}) dispersion coefficients have been used for modelling deviations from plug flow. They have been calculated using correlations from the literature for particulate beds [1]. In a similar way, gas-to-solid (h) and gas-to-wall (h_w) heat transfer have been accounted for using the corresponding coefficients [32]. The main physical properties used in the model are summarized in Table 2. The model was solved with the help of a code written in MATLAB based on `pdepe` function.

2.4. Modelling of the regenerative catalytic oxidizer

A 1D heterogeneous dynamic model has been used to simulate the regenerative catalytic oxidiser. The model is formed by the mass and energy balances of Table 1, which have been solved using the corresponding parameters obtained from specific correlations for the type of bed, properties and phenomena taking place in the oxidiser. This information can be found in previous works, where the model is explained in detail and validated with experimental data [28,7,8].

The oxidizer is formed of two bed towers and a combustion chamber in-between. Each tower contains a bed of honeycomb monolithic blocks forming two layers, one inert at the bottom and another catalytic at the top. The catalytic monoliths contain channels with a washcoat layer impregnated with Pd active phase. The catalyst decreases the ignition temperature of methane (T_{50} = 500ºC at GHSV = 135 000 h^{-1}) [7]. The oxidation of methane is modelled by a first order rate law with respect to methane; both internal (inside the washcoat layer) and external (gas film of the monolith channel) mass transfer resistances have been

Table 1
1D heterogeneous dynamic model for fixed beds.

Mass balance

$$\epsilon_b\frac{\partial c_i}{\partial t} = -\frac{\partial(uc_i)}{\partial z} + \epsilon_b D_{ie}\frac{\partial^2 c_i}{\partial z^2} + (1-\epsilon_b)\rho_S r_i$$

Energy balances

$$\epsilon_b\rho_G C_{PG}\frac{\partial T_G}{\partial t} = -\rho_G C_{PG} u\frac{\partial T_G}{\partial z} + \epsilon_b k_{Ge}\frac{\partial^2 T_G}{\partial z^2} - ah(T_G - T_S) - a_w h_w(T_G - T_w)$$

$$(1-\epsilon_b)\rho_S C_{PS}\frac{\partial T_S}{\partial t} = (1-\epsilon_b)k_S\frac{\partial^2 T_S}{\partial z^2} - ah(T_S - T_G) + (1-\epsilon_b)\rho_S r_i \Delta H_i$$

Initial conditions

$$c_i|_{t=0} = 0 \text{ and } T_G|_{t=0} = T_S|_{t=0} = T_{ini}$$

Boundary conditions

$$c_i|_{z=0} = c_{i0},\ T_G|_{z=0} = T_{G0}$$

$$\left.\frac{\partial c_i}{\partial z}\right|_{z=L} = \left.\frac{\partial T_G}{\partial z}\right|_{z=L} = \left.\frac{\partial T_S}{\partial z}\right|_{z=0} = \left.\frac{\partial T_S}{\partial z}\right|_{z=L} = 0$$

Where c_i is the methane concentration in the gas phase, and T_G and T_S are, respectively, the gas and solid temperatures.

Table 2
Physical and chemical properties of the fixed bed adsorption/desorption unit.

Bed length (L)	0.145
Bed diameter (D)	0.060
Particle diameter, d_p (mm)	3
Bed porosity, ϵ_b	0.43
Solid density, ρ_S (kg/m^3)	758
Solid heat capacity, C_P (J/kg K)	1040
Solid thermal conductivity, k_S (W/m K)	0.5
Heat of adsorption, -ΔH_i (kJ/mol)	17

considered using the following equations:

$$-r_i = K_{w,gl} c_{Gi} \tag{2}$$

$$\frac{1}{K_{w,gl}} = \frac{1}{\eta k_w R T_S} + \frac{1}{(1-\epsilon_b)\rho_S a k_f} \tag{3}$$

where $k_w = 1.56e^{-9622/T_S}$ mol/kg$_{cat}$ s Pa is the reaction rate constant, η is the internal effectiveness factor (estimated using the physical and textural properties for the catalyst) and k_f is the gas-film mass transfer coefficient [8].

The solving of the model predicts the evolution upon time of the bed concentration and temperature profiles. The software COMSOL Multiphysics, based on the Finite Element Method, has been used to solve the model equations upon time. The switch of the flow direction has been simulated by a change in the sign of the velocity vector ($u > 0$ for one half-cycle and $u < 0$ for the following one) and a switch of the boundary conditions of Table 1 [28].

3. Results and discussion

3.1. Bench-scale adsorption

The first series of experiments consisted in the determination of the adsorption break curves by the step-response method. The break curves were obtained at 100 kPa, 293 K and a space velocity (WHSV) of 15.1 mol/kg h (gas flow rate 1 NL/min) for different methane feed concentrations in air (0.20–0.50 vol%). Fig. 1 shows the evolution with time of the outlet methane concentration, starting from clean adsorbent and ending with saturated adsorbent. The shape of the curves represents the dynamics of the fixed bed, and information regarding the equilibrium (adsorption isotherm) and kinetics (mass transfer) can be obtained from them Fig. 2.

At the end of each test, the adsorbent was completely saturated with methane, i.e., at equilibrium; the concentration of adsorbed methane ($q^*_{CH_4}$) can be calculated from a mass balance to a single break curve:

$$q^*_{CH_4} = \frac{y_{i0} F_0}{W} \int_0^{t_{end}} \left(1 - \frac{c_i}{c_{i0}}\right) dt \tag{4}$$

Where y_{i0} is the mole fraction of methane in the feed and F_0/W is the space velocity (WHSV).

The equilibrium adsorption isotherm is obtained by representing, for all the tests, $q^*_{CH_4}$ as a function of the partial pressure of methane in the gas feed, p_{CH_4} (Fig. 3a). The data have been fitted to a linear adsorption isotherm, $q^*_{CH_4} = K_{ads}\ p_{CH_4}$, with slope $K_{ads} = 8.77{\cdot}10^{-3}$ mol/kg kPa (dotted line in Fig. 3a, regression coefficient, $R^2 = 0.95$). This type of isotherm is typical for weak adsorption and at low partial pressures. These equilibrium adsorption results have been compared to data from the literature, as explained in the following paragraphs.

The equilibrium adsorption capacities of methane and nitrogen gases on active carbon were measured in a Micromeritics ASAP2020 device by Rufford et al. [36]. In their tests, pure gas was used and the adsorption capacity was measured at increasing total pressures. However, in the step-response tests carried out in the present work, methane/nitrogen mixtures in the range 0.20–0.50 vol% CH_4 were considered at a total pressure of 100 kPa. Consequently, simultaneous methane and nitrogen adsorption is taking place. The multi-component equilibrium Langmuir adsorption isotherm is suitable for predicting mixture equilibrium adsorption capacities using pure-gas adsorption data for the case of low partial pressure of one gas (methane):

$$q^*_{CH_4} = \frac{q_s b_{CH_4} p_{CH_4}}{1 + b_{CH_4} p_{CH_4} + b_{N_2} p_{N_2}} \approx K_{ads}\ p_{CH_4} \tag{5}$$

Where $q_s = 0.995$ mol/kg, $b_{CH_4} = 1.166{\cdot}10^{-2}$ kPa^{-1} and $b_{N_2} = 2.75{\cdot}10^{-3}$ kPa^{-1} have been fitted from the data of Rufford et al. [36]. Considering the concentration range of the step-response experiments ($p_{CH_4} < 0.5$ kPa and $p_{N_2} \approx 100$ kPa), the term $b_{CH_4} p_{CH_4} \approx 0$ and $b_{N_2} p_{N_2}$ is approximately constant, resulting in a multi-component linear adsorption isotherm with slope $K_{ads} = q_s b_{CH_4}/(1 + b_{N_2} p_{N_2}) = 9.07{\cdot}10^{-3}$ mol/kg kPa. This slope is only 3% higher than that fitted in the present work to the data of the step-response method. The predictions of Eq. (5) have been depicted in Fig. 3a (solid line).

The rate of mass transfer is, together with the adsorption equilibrium, a key factor to consider the scale-up of adsorption processes. In porous adsorbents, there are three possible mass transfer resistances: gas film, pore diffusion and surface diffusion resistances [10]. Active carbons are microporous materials with high surface area and small pore size (respectively, 871 m^2/g and 1.7 nm for the adsorbent of this work). In this type of adsorbents, surface diffusion is typically the controlling mass transfer mechanism, since pores are so small that for the molecules is difficult to escape from the solid force field and they move by hopping from one point to another [23,40].

In the present work, the break curves obtained by the step response method have been fitted to the 1D heterogeneous dynamic model introduced in the Materials and Method section (mass balance of Table 1 and Eq. (1)). The only unknown parameter of the model is the overall mass transfer coefficient (K_{Li}), which has been fitted to the experimental data by least-square regression; the adsorption capacity has already been determined has explained above. As depicted in Fig. 1 (lines), the fitted model agrees well with the experimental data. The fitted overall mass transfer coefficients are shown in Fig. 2b. It can be observed that the values are very similar for all the cases, with a slight deviation for the case of 0.20 vol% methane. The average value for the range 0.30–0.50 vol% methane is $K_{Li} = 0.221$ s^{-1}. In the following, the overall mass transfer coefficient is decomposed as a function of the different mass transfer resistances: gas film, pore diffusion and surface diffusion resistances. The first two ones can be estimated using correlations and properties of the gas and adsorbent. The later one has been determined

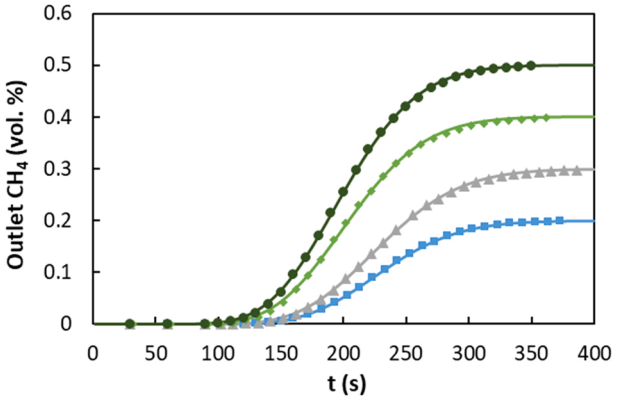

Fig. 2. Methane adsorption break curves. Methane feed concentration (in vol %): 0.20 (■), 0.30 (▲), 0.40 (◆) and 0.50 (●). Temperature: 293 K. Space velocity: WHSV 15.1 mol/kg h. Symbols: experiments. Lines: model fitting.

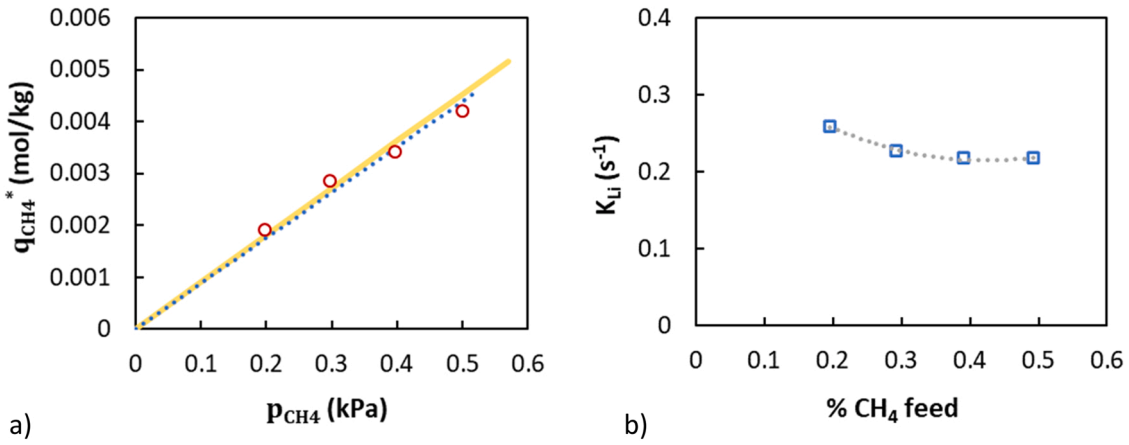

Fig. 3. a). Equilibrium methane adsorption isotherm in nitrogen at 100 kPa and 293 K. (Symbols: experiments, this work. Dotted line: fitting, this work. Solid line: Langmuir multi-component isotherm, pure-gas adsorption data of [36]). b). Overall methane mass transfer coefficient at 100 kPa and 293 K (Symbols: experiments. Lines: fitting).

indirectly by subtracting the first two one from the overall.

The gas film resistances, first summation of Eq. (6), has been estimated as 0.37 s (which is only 8.2% of the overall resistance, $1/K_{Li} = 4.52$ s) [10]:

$$\frac{1}{K_{Li}} = \frac{\epsilon_b}{6}\frac{\Lambda}{(1-\epsilon_b)k_f}\frac{d_P}{} + \frac{1}{K_{int}} \tag{6}$$

where $\epsilon_b = 0.43$ is the bed porosity, $\Lambda = \rho_S(1-\epsilon_b)q_{i0}/\epsilon_b c_{i0} = 21.5$ is the adsorption stoichiometry parameter, $k_f = 0.022$ m/s is the pellet film mass transfer coefficient (determined using a correlation from Sherwood number [10]).

The intraparticle mass transfer coefficient (K_{int}) can be divided into two contributions: pore and surface diffusion (respectively, the first and second summations in Eq. (7)) [10].

$$K_{int} = \frac{60(1-\epsilon_b)D_{Pi}}{\epsilon_b}\frac{\Lambda}{d_P^2} + \frac{60D_s}{d_P^2} \tag{7}$$

Pore diffusion takes place in the gas phase inside the adsorbent pores. It is characterized by the pore diffusion coefficient, $D_{Pi} = 3.44{\cdot}10^{-8}$ m^2/s, determined as a combination of Knudsen and molecular diffusion mechanisms [10]:

$$D_{Pi} = \frac{\epsilon_P}{\tau_P}\left[\frac{3}{4}\frac{}{r_{pore}}\left(\frac{\pi M_{wi}}{2RT}\right)^{1/2} + \frac{1}{D_{AB}}\right]^{-1} \tag{8}$$

where $\tau_P = 4$ is the tortuosity of the pore network, $\epsilon_P = 0.397$ is internal porosity of the adsorbent, $r_{pore} = 0.85$ nm is the average micropore radius, $M_{wi} = 0.016$ kg/mol is the molecular weight of methane and $D_{AB} = 2.1{\cdot}10^{-5}$ m^2/s is the methane/air molecular diffusion coefficient. For the given adsorbent material and operating conditions, the pore diffusion resistance term, $60(1-\epsilon_b)D_{Pi}/\epsilon_b \;\; \Lambda \;\; d_P^2$, is estimated as 0.014 s^{-1}, which contributes only to a 5.9% of the total intraparticle resistance ($K_{int} = 0.240$ s^{-1}).

The surface diffusion resistance term, $60D_s/d_P^2 = 0.226$ s^{-1}, has been determined by subtracting the contribution of the other resistances estimated previously from the overall resistance. This value is similar to other reported in the literature for activated carbons [43]. It has been demonstrated that the surface diffusion is the controlling mass transfer mechanism with a contribution of 86%.

3.2. Bench-scale desorption

Methane desorption has been studied in the fixed-bed device, starting with the adsorbent completely saturated with methane at 293 K. The desorption has been forced by feeding hot air at 358 K (the temperature of the bed has also been increased to 358 K) as sweeping gas. This shifts the adsorption equilibrium, promoting methane desorption, and the appearance of a peak in methane outlet concentration, as shown in Fig. 4. These tests have been planned to study the influence on the desorption process of two parameters: methane saturation concentration in the previous adsorption step (0.20–0.50 vol%) and sweep air flow rate (0.2–0.55 NL/min, corresponding to WHSV in the range

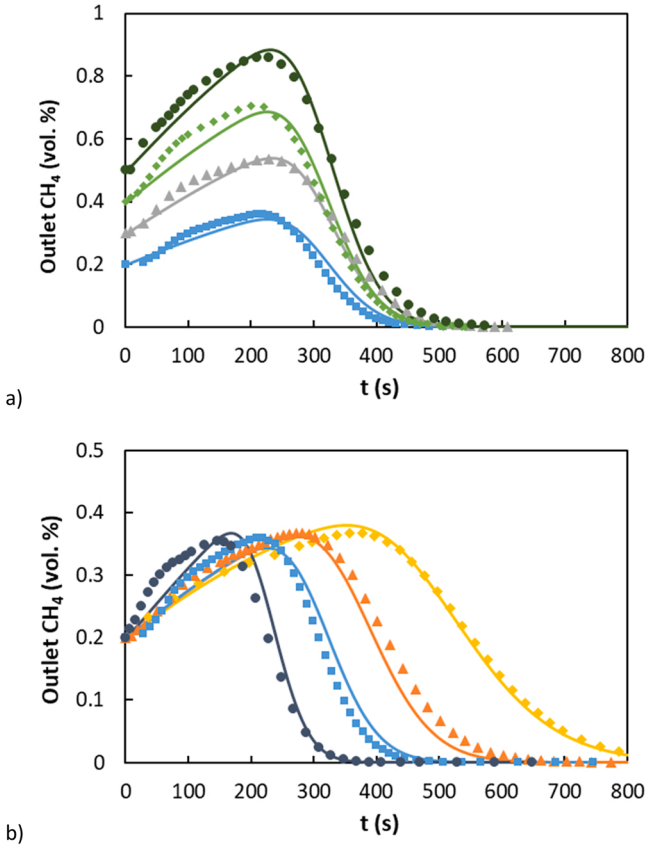

Fig. 4. Methane desorption: a). Influence of methane saturation concentration (in vol%): 0.20 (■), 0.30 (▲), 0.40 (◆) and 0.50 (●). Space-velocity: WHSV 6.0 mol/kg h. b). Influence of sweep air flow rate, WHSV: 3.0 (◆), 4.7 (▲), 6.0 (■) and 8.5 mol/kg h (●). Methane saturation concentration: 0.20 vol%. Symbols: experiments. Lines: model fitting.

3.0–8.5 mol/kg h).

All the desorption curves exhibited an increase in methane outlet concentration above the corresponding feed concentration of the adsorption step. This demonstrates experimentally that NORIT GF-40 is an adsorbent suitable for the concentration of lean methane sources. In addition, the curves have a similar parabolic shape: first, the outlet concentration increases up to a maximum and, then, decreases towards cero. The curves obtained for different methane saturation concentrations (Fig. 4a) present a maximum point at ca. 200 s, for all the curves, with a concentration value 1.8 times the corresponding adsorption methane saturation concentration (e.g., $c_{i,max}/c_{i0} = 1.8$). The aim of the adsorption operation is to concentrate methane, so there is no reason to extend the desorption step beyond the point where the outlet concentration equals the adsorption feed concentration. This point has been determined from the desorption curves of Fig. 4a and it has been found to be very close for all the tests, with average desorption time of 327 s. The average outlet methane concentration up to this time is also very similar for all the tests, 1.48 times the corresponding adsorption methane saturation concentration. In fact, all the curves in Fig. 4a, obtained for the same air flow rate and temperature, overlap when represented in terms of c_i/c_{i0}. These similitudes are due to the linear adsorption isotherm, which means that the amount of adsorbed methane at the beginning of each test is proportional to the feed concentration.

The second set of experiments, shown in Fig. 4b, studies the influence of the air flow rate (WHSV = 3.0–8.5 mol/kg h). The saturation methane concentration was fixed to 0.20% for all the tests and the desorption temperature maintained in 358 K. A decrease in the flow rate produced a shift in the concentration curve towards higher time values and vice versa. However, it should be noted that the maximum outlet concentration value remains practically constant, at ca. 1.8 times the saturation concentration. The desorption time required to achieve an outlet concentration equal to the saturation concentration was also calculated, as shown in Fig. 5. This parameter has been correlated as a function of the stoichiometric time, $\theta = \left(q^*_{i0}/y_{i0}\right)_{ads}/(F_0/W)_{des}$, where q^*_{i0} and y_{i0} are, respectively, the adsorbed and gas concentrations at the end of the adsorption step and F_0/W is the space velocity of the desorption step. The linear fitting gives a slope of 0.5 (R^2 =0.98), which means that only 50% of the adsorbed methane can be recovered in the desorption step with a higher concentration than that of the feed.

The fixed-bed desorption experiments have also been modelled using the 1D heterogeneous dynamic model presented in the Materials and Methods section. In this case, the mass and energy balances have been solved (non-isothermal model), since the bed was initially at 293 K (end of adsorption step) and the desorption step was carried out with sweep air and tube wall temperature at 358 K. This change in temperature produced a decrease of the equilibrium adsorption constant from 8.77 10^{-3} at 293 K to 2.47 10^{-3} mol/kg kPa at 358 K (enthalpy of adsorption −17 kJ/mol) [18]. Other temperature-dependant properties, such as, density or diffusion coefficients, have been modelled using the correlations proposed in the literature [32].

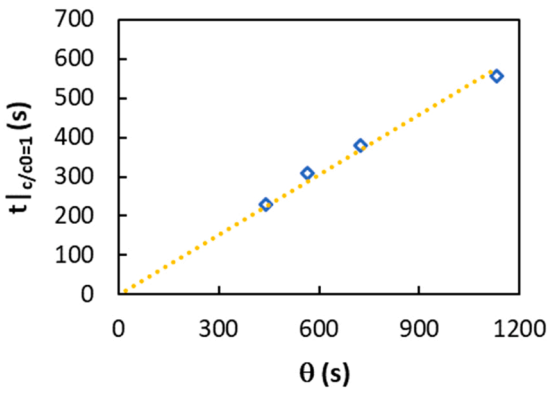

Fig. 5. Correlation of desorption time and stoichiometry time: $t_{c/c_0=1} = 0.5\theta$.

The linear driving force model has been used to represent mass transfer between the gas and solid adsorbent. Since the extraparticle (or film) resistance depends on temperature and gas flow rate (considerably lower in the desorption tests), this resistance needs to be revaluated. Eqs. (6)–(8) have been used to estimate the individual resistances and calculate the overall mass transfer coefficient for the desorption tests. The model has been used to simulate (without data fitting) the experiments presented in Fig. 4; in which results are depicted as lines. It can be observed that the model is able to predict the outlet methane concentration very well. The shape of the curve and the placement of the maximum is predicted accurately for all the cases.

According to these results, it can be concluded that the dynamics of the fixed bed, both for adsorption and desorption, can be described accurately using the proposed 1D heterogeneous dynamic model. This model can be used for the design and scale-up of adsorption/desorption units.

3.3. *Integrated temperature-swing adsorption-regenerative catalytic oxidizer process*

The integrated process consists of a temperature-swing adsorption (TSA) and a regenerative catalytic oxidizer (RCO) units connected, as shown in Fig. 6. The emission considered for the scale-up consists of 0.20 vol% methane in air at 293 K and 100 kPa with a total flow rate of 4.50 Nm^3/s (200 mol/s). This stream is representative of many lean methane emissions, such as those found in the ventilation air of coal mines, landfills, etc. The emission is introduced in the first fixed-bed acting as adsorber. At these conditions, methane is adsorbed on the activated carbon until saturation. Then, the role of this bed is changed to desorption, as indicated in the second bed of Fig. 6. The desorption step requires a sweep air at a moderate temperature (358 K) to promote methane desorption. This sweep air can be obtained from the air exhaust of the RCO, which is typically in the range 353–373 K. If needed, a make-up air can be used to adjust flow rate and temperature. The thermal integration of the TSA and RCO units is critical for the economy of the process. Thus, the use of residual heat from one of the units to supply the energy requirements of the other would reduce the operating costs considerably.

The effluent of the desorption unit, which consists of a stream concentrated in methane, is fed to the RCO unit. As explained before, methane concentration of this stream is not constant upon time. For the case of an adsorption methane saturation concentration of 0.20 vol%, the effluent concentration would increase from 0.20 vol% up to a maximum at 0.36 vol% and then decrease. As depicted in the experimental results of Fig. 4, the maximum concentration is approx. 1.8 times the methane concentration in the emission treated. The desorption is stopped when the concentration of methane in the effluent falls below 0.20 vol%. The average concentration within this operating period is 0.30 vol% methane (1.48 times the saturation concentration).

The RCO is a reactor operated unsteadily, therefore it is necessary to determine how this evolution in the concentration of the desorption effluent (which is the reactor feed) affects its stability and operating window. The study of this influence by means of computer simulations of the RCO is one of the objectives of the present work. The RCO has been designed for a switching time of 90 s, which corresponds to a cycle time of 180 s (a cycle consists of one direct half-cycle and one reverse half-cycle). For this reason, and in order to achieve a stable pseudo-steady state in the overall process, the integration of TSA and RCO units requires a synchronization of their operation. Two types of integration couplings have been considered in this work, as depicted in Fig. 7. For integration type 1, the desorption step is designed with an operating time equal to a cycle of the regenerative oxidizer, i.e. 180 s or two switches of the flow direction ($N_{SW} = 2$). For type 2, the desorption step is longer and amounts 360 s or two cycles of the oxidizer ($N_{SW} = 4$). In both types of couplings, the evolution of the methane concentration

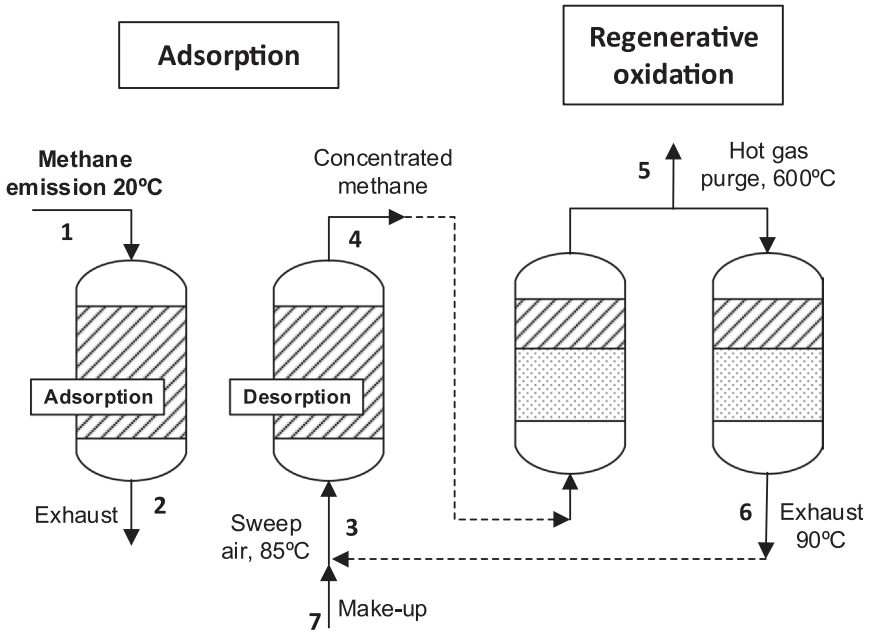

Fig. 6. Flowsheet of the integrated TSA-RCO configuration.

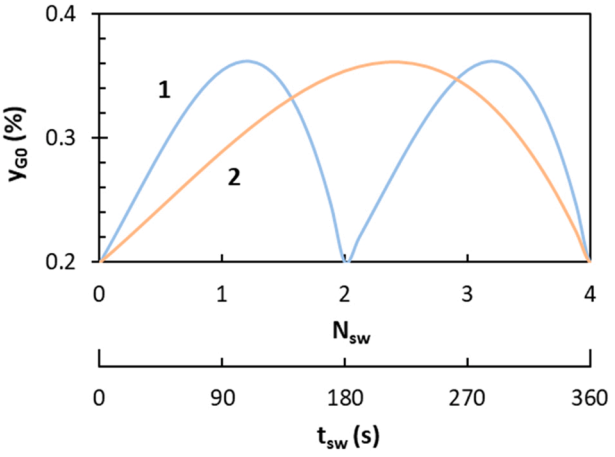

Fig. 7. Integration of adsorption/desorption and regenerative catalytic oxidizer units: periodic evolution of the methane concentration in the RCO feed for coupling type 1 ( ) and 2 ( ).

fed to the RCO with time was obtained with the model whose predictions are shown in Fig. 4. These profiles of the methane concentration are repeated periodically from the beginning to the end of the simulation of the RCO unit, so that successive desorption cycles can be simulated.

Summarizing, the integration of TSA and RCO units takes place at two levels: mass and energy integration. Mass integration is produced when both units are designed and coupled through the stream of the desorption effluent. Energy integration is achieved by using the sensible heat of the RCO exhaust as sweep air in the desorption step.

3.4. Design of the adsorption-desorption unit

In this section, the design of the adsorption-desorption unit as part of the integrated TSA-RCO process is addressed. The emission to be treated has a flow rate of 4.50 Nm^3/s (200 mol/s) and a methane concentration of 0.20 vol%.

In the previous section, two types of couplings were proposed for the integrated process with desorption times of 180 and 360 s, respectively, for type 1 and 2 couplings. Considering the same cycle times for the adsorption and desorption steps, the weight of adsorbent can be calculated from a mass balance to the adsorption step:

$$W = \frac{F_{0,ads} y_{i0} t_{cy}}{q^*_{i0}} \tag{9}$$

where $F_{0,ads} = 200$ mol/s is the flow rate of the emission, and $y_{i0} = 2{\cdot}10^{-3}$ and $q^*_{i0} = 0.00175$ mol/kg are the saturation concentrations, respectively, of the gas and solid phases. The required weight of adsorbent is different for type 1 ($t_{cy} = 180$ s) and type 2 ($t_{cy} = 360$ s) couplings, respectively, 4.12 10^4 and 8.25 10^4 kg.

For the sizing, the bed diameter (D) is limited to a maximum of 3.5 m for practical purposes. Considering a superficial velocity for the gas of ca. 0.2 m/s n.t.p. (too high gas velocity would increase pressure drop and, hence, the pumping costs), it is determined that 2 parallel beds are required to process all the gas flow rate. These two beds can be operated staggered in time to increase the efficiency of the operation. The bed length is now obtained from the weight of adsorbent and geometrical considerations: 5 m for type 1 and 10 m type 2 couplings.

The desorption step operates with the same weight of adsorbent (W) and cycle time (t_{cy}). At the end of the desorption step, the bed is not completely free of methane, as indicated by the ratio of time to stoichiometric time (θ) determined experimentally, $t_{c/c_0=1}/\theta = 0.5$. Using this ratio in the following expression (Eq. 10) and setting $t_{c/c_0=1} = t_{cy}$, the flow rate of the sweep air required in the desorption step ($F_{0,des}$) is 100 mol/s (for type 1 and 2 couplings).

$$F_{0,des} = \frac{(q^*_{i0}/y_{i0})W}{(t_{cy}/0.5)} \tag{10}$$

The dimensions of desorption and adsorption beds are the same, as this role changes every cycle. In the desorption step, the superficial velocity of the gas is calculated as 0.1 m/s n.t.p. (0.12 m/s measured at 358 K), which is lower than that of the adsorption step, so pressure drop will also be lower.

The results of the adsorber sizing are summarized in Table 3. It should be noted that there are three equal sets of two parallel beds in the system, one for each step of the TSA process: adsorption, desorption and regeneration. The later step involves the operations required to re-establish the conditions needed at the beginning of the adsorption step (e.g., cooling, purge, etc.).

Table 3
Main design specifications and parameters of the adsorber and oxidizer.

	Adsorber	Oxidizer
Feed flow rate (Nm^3/s)	4.50	2.25
Methane design concentration (vol%)	0.20	0.30
Superficial velocity (m/s)	0.2/0.1	1
Switching time (s)	180/360	90
Number of beds	2 each step (6 total)	2
Bed length (L)	5/10	0.60
Bed diameter/side (D)	3.5	1.50
Particle diameter/channel side (mm)	3	1.8
Bed porosity, ϵ_b	0.43	0.64
Solid density, ρ_S (kg/m^3)	758	2300
Solid heat capacity, C_P (J/kg K)	1040	865
Solid thermal conductivity, k_S (W/m K)	0.5	1.6
Heat of adsorption/reaction, $-\Delta H_i$ (kJ/mol)	17	802.5

3.5. Design of the regenerative catalytic oxidizer unit

The design of the integrated RCO unit has been done considering that the feed of the RCO is the effluent of the desorption step of the TSA unit. As mentioned before, this stream has a flow rate of 2.25 Nm^3/s (100 mol/s) and methane concentration varying according to Fig. 7.

For simplicity, the sizing of the RCO unit has been done considering constant methane concentration and equal to 0.30 vol%. In the following section, the resilience of the design towards a change in methane concentration will be investigated and tested.

As sketched in Fig. 6, the oxidizer is formed by two parallel beds of square cross section and a combustion chamber placed in-between. The beds are made of monolithic blocks with square channels and a cell density of 100 cpsi (1.8 mm of channel size and 64% of bed porosity). There are two main design variables in this system, bed side and length.

The bed side has been calculated considering a superficial velocity of ca. 1 m/s (n.t.p.), which is a compromise value (higher superficial velocities lead to higher pressure drop, while lower ones to beds of large cross section) [24]. Considering this and the feed flow rate a bed side of 1.50 m is obtained.

The bed length has been determined, so that stable operation is achieved for a given design switching time of 90 s. This value has been selected as recommended in the bibliography (high switching times lead to higher bed lengths, while very low ones are negative because of the bypass of unconverted methane from the inert beds when the flow direction is switched) [26,28]. The calculations have been done with the help of the model introduced in Section 2.3. Thus, a given set of design specifications (summarized in Table 3), simulations are carried out up to the pseudo-steady state for increasing bed lengths. The minimum bed length resulting in stable operation of the RCO (methane converted and steady temperature with no overheating) is chosen as the design bed length. More details about the design can be found elsewhere [8,28]. According to this procedure, it has been determined that each oxidizer requires a bed of 0.60 m length made of two layers of monolithic blocks: one inert layer of 0.30 m and one catalytic layer also of 0.30 m. The catalytic monolithic blocks are geometrically identical to the inert ones, but impregnated with active phase, so that the ignition temperature of methane is lowered to ca. 500ºC. Using this configuration, methane conversion above 99% can be achieved.

3.6. Assessment of the integrated TSA-RCO

The aim of this section is to study the performance of the integrated TSA-RCO process shown in Fig. 6 by means of simulations. More specifically, the study of the influence of the oscillating methane concentration in the feed to the RCO on its stability and operating window.

The stability of the RCO alone has been evaluated within a feed with constant concentration (0.30 vol%), which has been set as the basis for comparison with other concentrations. Fig. 8a shows the temporal evolution of the gas temperature of the middle point of the oxidizer (i.e., in the combustion chamber). This temperature is the highest of the oxidizer, so it is very useful as a measurement of the oxidizer's performance, as explained below. N_{sw} is the number of flow switches (i.e. multiply by the switching time, 90 s, to transform it into time).

For the case of operation without hot gas withdrawal, the gas temperature of the mid-point increases progressively to a value close to 700ºC. This is due to an excess of heat accumulation inside the oxidizer, which increases the temperature above the operating target for RCO. The excess heat can be extracted by the withdrawal of a fraction of the hot gas stream from the centre of the oxidizer, or with a heat exchanger. The assessment of the best control strategy is discussed in the bibliography [24,28]. As shown in Fig. 8a, the withdrawal of hot gas in adequate amount succeeds in controlling the overheating, and the temperature stabilized at a lower value. However, if too much hot gas was extracted (>10%), the autothermal behaviour would be broken and the oxidizer would extinguish. The recommended operating point corresponds to a hot gas withdrawal of 8% and a temperature of 600 ºC. This value is used in the following simulations.

The influence on the stability of the dynamics of the feed concentration is studied in Fig. 8b. The RCO feed has been varied according to the outlet of the TSA system during the desorption step. Two types of couplings have been considered, as depicted in Fig. 7. Both types of adsorber-reactor coupling resulted in stable operation of the RCO, though there are differences in the observed behaviour. For coupling type 1, the mid-point temperature increased a bit more at the beginning, but then it decreased to the same pseudo-steady state value of that for

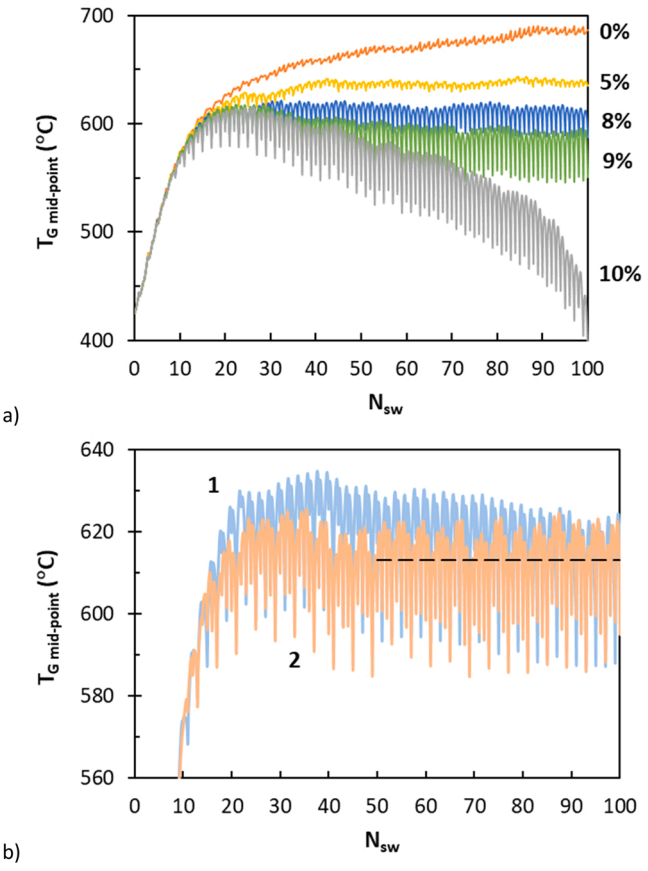

Fig. 8. Integrated TSA-RCO process. a). Influence of the fraction of hot gas withdrawal on the stability of the RCO (0.30 vol% methane): 0 ( ), 5% (, 8% ( ), 9% ( ) and 10% ( ). b). Assessment of the stability for type 1 ( ) and type 2 ( ) couplings (0.20 vol% methane, hot gas withdrawal = 8%, dashed lines indicate average temperature at the pseudo-steady state).

coupling 2, at ca. 613ºC. Thus, type 1 coupling is characterized by faster dynamics, concentration varying across 180 s ($N_{SW} = 2$), instead of the 360 s ($N_{SW} = 4$) of type 2 coupling. This explains the higher sensitivity of type 1 coupling to the maximum methane concentration (0.36 vol%), which is responsible of the accumulation of the excess heat and, hence, the observed temperature increase. Conversely, even if the maximum methane concentration value is the same, the dynamics in the feed concentration of type 2 coupling covers 4 half-cycles of the RCO, which clearly softens the influence at the mid-point temperature.

Fig. 9 provides a better insight into the performance of type 2 coupling. Temperature and axial concentration profiles obtained at the pseudo-steady state (direct half-cycle, 0–90 s) are depicted for two methane feed concentrations to the TSA-RCO process: 0.20 (Fig. 9a) and 0.50 vol% (Fig. 9b). Thanks to the concentration of the TSA step, methane concentration entering the RCO is higher than the feed one, as shown in Fig. 7. To illustrate the dynamic nature of the RCO, in each plot, profiles are depicted for every 20 s; these profiles move upon time in the direction of the gas flow, as indicated by the arrows. The placement of the catalytic beds is also indicated with the help of vertical dashed lines.

On entering the RCO, the gas feed is heated using the energy stored in the monolithic bed. The consumption of sensible heat from the bed causes a decrease in the bed temperature, which is observed as a movement in the temperature profiles. The flow direction is reversed before an excessive amount of heat is drained from the bed. The heat of combustion is released in the catalytic beds, producing a remarkable increase in temperature. Given the symmetry of the device, the highest temperature is achieved in the centre of the oxidizer, where a fraction of the gas stream is purged as part of the control system to prevent overheating. The fraction of hot gas withdrawal is 8% for a methane feed of 0.20 vol% and 24% for 0.50 vol%. The second half of the oxidizer is mainly used to store the energy of the combustion gases in the following cycle. The temperature and concentration profiles indicate that the reaction is initiated at ca. 400ºC. Thus, for the case of 0.20 vol% methane and the end of the half-cycle, it can be observed that the ignition is postponed to the middle of the catalytic bed, since the temperature at the entrance is not high enough ($T_{z=0.3\ m}$ = 200ºC, while $T_{z=0.45\ m}$ = 400ºC). Because of this delayed ignition, methane conversion is not completed in the first catalytic bed, but in the second one. On the contrary, for the case of 0.50 vol%, the bed temperature raised up to 787ºC, due to a higher amount of heat being released, so all methane was converted in the first catalytic bed.

For the case of 0.20 vol% methane (Fig. 9a), the progressive change in the methane concentration in the feed during this RCO cycle from 0.20 to 0.36 vol% causes an increase in the heat released in this cycle (adiabatic temperature changes from 55 to 100ºC). However, this temperature increase has little impact on the performance of the RCO. Methane conversion is complete, and the shape of the temperature profiles shows no signs of overheating. The RCO operation is intrinsically based on the regenerative storage of heat between cycles. This capacity is being used here to store the excess heat released by the reaction when methane concentration increases. Thus, the extra amount of heat stored is used to prevent the extinction of the RCO when methane concentration decreases. Since this increase and decrease of methane concentration is exactly repeated cycle after cycle, the pseudo-steady state characterized by the occurrence of the same temperature evolution is finally reached. The simulations carried out for the integrated TSA-RCO process show that these two processes can be effectively integrated with efficient and stable operation.

The performance of the TSA-RCO process has also been explored for other methane feed concentrations in the range 0.20–0.50 vol%. These simulations are summarized in Fig. 10 in terms of the fraction of hot gas withdrawal needed for stable operation, i.e., with a steady reactor temperature resulting from a balance between the heat released and extracted (higher fractions would result in extinction and lower ones in overheating). These critical fractions of hot gas withdrawal have been determined following the procedure explained in Fig. 8a. Thus, it is obtained that on increasing methane feed concentration, the fraction of hot gas withdrawal must be increased to extract from the oxidizer the additional heat released by the reaction. The advantages of using an integrated adsorber-reactor (with type 2 coupling) with respect to the case of the single reactor without methane concentration by adsorption is depicted in Fig. 10. Thus, it has been found that the integrated absorber-reactor is able of increasing the actual methane concentrated entering in the reactor and, for this reason, the fraction of hot gas withdrawal must be increased. This is observed for all the

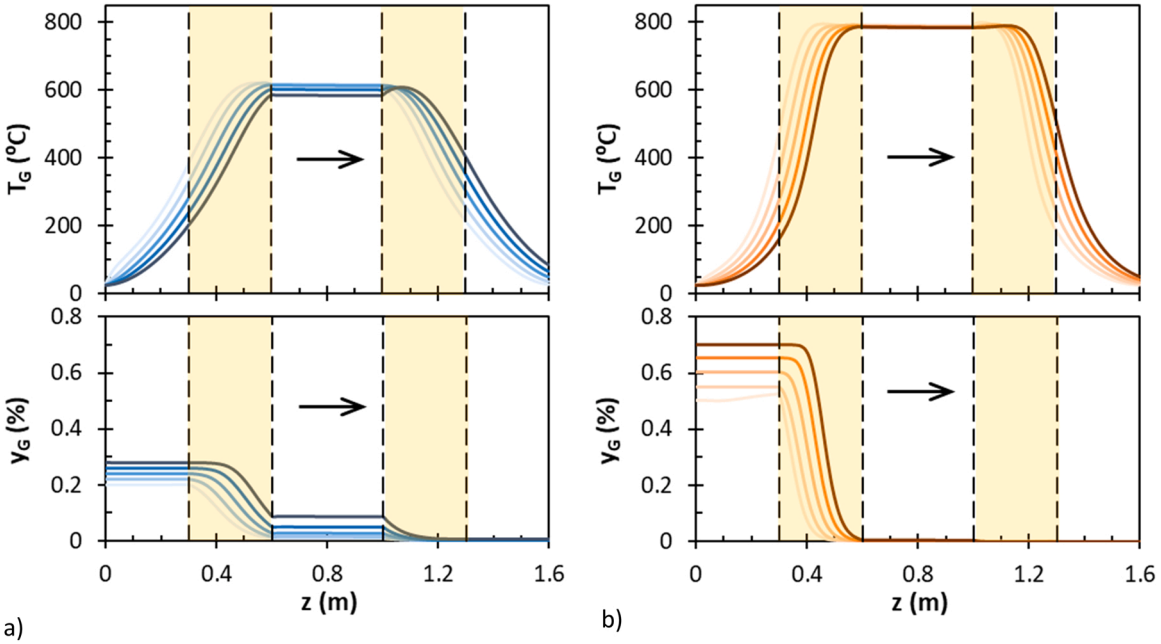

Fig. 9. Evolution of temperature and concentration profiles at the pseudo-steady state (direct half-cycle) for type 2 coupling (one profile every 20 s; flow direction indicated by the arrow; dashed vertical lines delimit the boundaries of the catalytic bed). Methane feed concentration to the TSA-RCO process: 0.20 (a) and 0.50 vol % (b).

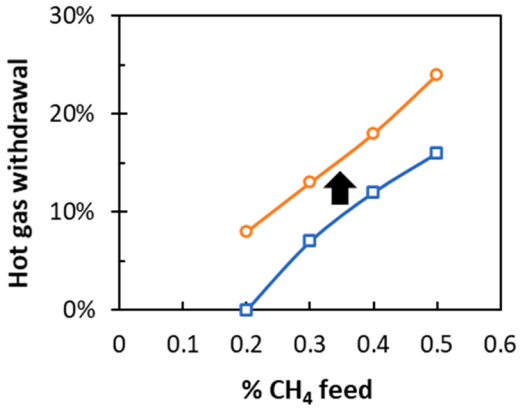

Fig. 10. Hot gas withdrawal required for stable operation of the RCO: (□) without adsorber and (○) with integrated adsorber (type 2 coupling).

concentrations considered, producing a raise in the operating curve of the critical fraction of hot gas withdrawal, e.g., for 0.50 vol% methane, the fraction of hot gas withdrawal increased from 16% to 24%.

The integrated adsorber-reactor not only increases the operating window regarding methane concentration, but also makes it is easier the thermal harnessing of methane. Thus, since the fraction of hot gas withdrawal must be increased the amount of heat extracted and harnessed from the reactor increases.

4. Conclusions

The treatment of lean methane emissions in an integrated adsorption-regenerative catalytic oxidation process has been modelled and a treatment unit designed.

The adsorption/desorption step was studied experimentally in a fixed bed. It has been concluded that activated carbon (Norit GF-40) is a suitable adsorbent for methane, though the adsorption capacity is low at lean conditions (0.20–0.50 vol% methane); the adsorption equilibrium data followed a linear isotherm with K_{ads}= 8.77 10^{-3} mol/kg kPa at 293 K. The adsorption dynamics was fitted to the linear driving force model with surface diffusion resistance $15D_s/r_p^2 = 0.226\ s^{-1}$ at 293 K. Temperature swing desorption tests at 358 K demonstrated that methane can be concentrated up to a maximum of 1.8 times the adsorption methane saturation concentration. As expected, methane concentration in the desorbed stream showed a parabolic profile with a maximum. The influence of this dynamics on the performance of the regenerative catalytic oxidizer when integrated with the adsorption/desorption operation has been studied by means of simulations for a unit designed for the treatment of an emission of 4.50 Nm^3/s flow rate with 0.20 vol% methane concentration. Methane is concentrated in the adsorbers to an average concentration value of 0.30 vol% with a flow rate of 2.25 Nm^3/s. Then, this stream is completely converted in the regenerative catalytic oxidizer.

Results indicate that, given its heat regenerative capacities, the oxidizer can handle the change of methane concentration produced in the adsorber without affecting its performance and stability.

CRediT authorship contribution statement

Ukrit Chaemwinyoo: Investigation, formal analysis. **Pablo Marin:** Conceptualization, Supervision, Data curation, Methodology, Writing – original draft. **Claudia Fernández Martín**: Supervision, Methodology, Writing – review and editing. **Fernando V. Diez:** Conceptualization, writing – review and editing. **Salvador Ordóñez:** Funding acquisition, conceptualization, supervision, writing – review and editing.

Declaration of Competing Interest

The authors declare that they have no known competing financial interests or personal relationships that could have appeared to influence the work reported in this paper.

Acknowledgements

This work has been financed by the Research Fund for Coal and Steel of the European Union (METHENERGY PLUS, contract 754077). Ukrit Chaemwinyoo thanks the Erasmus+ program of the European Union.

References

[1] Albright, L., Albright's Chemical Engineering Handbook. 1st Edition ed, ed. L. Albright. 2008, Boca Raton: CRC Press.
[2] A.A. Barresi, G. Baldi, D. Fissore, Forced unsteady-state reactors as efficient devices for integrated processes: case histories and new perspectives, Ind. Eng. Chem. Res. 46 (25) (2007) 8693–8700.
[3] V. Bukarica, Ž. Tomšić, Energy efficiency policy evaluation by moving from techno-economic towards whole society perspective on energy efficiency market, Renew. Sustain. Energy Rev. 70 (2017) 968–975.
[4] M.A. Carreon, Molecular sieve membranes for N2/CH4 separation, J. Mater. Res. (2017) 1–12.
[5] D.L. Cluff, G.A. Kennedy, J.G. Bennett, P.J. Foster, Capturing energy from ventilation air methane a preliminary design for a new approach, Appl. Therm. Eng. 90 (2015) 1151–1163.
[6] S. Eyer, N.P. Stadie, A. Borgschulte, L. Emmenegger, J. Mohn, Methane preconcentration by adsorption: a methodology for materials and conditions selection, Adsorption 20 (5–6) (2014) 657–666.
[7] J. Fernández, P. Marín, F.V. Díez, S. Ordóñez, Coal mine ventilation air methane combustion in a catalytic reverse flow reactor: influence of emission humidity, Fuel Process. Technol. 133 (2015) 202–209.
[8] J. Fernández, P. Marín, F.V. Díez, S. Ordóñez, Combustion of coal mine ventilation air methane in a regenerative combustor with integrated adsorption: Reactor design and optimization, Appl. Therm. Eng. 102 (2016) 167–175.
[9] D. Gewald, K. Siokos, S. Karellas, H. Spliethoff, Waste heat recovery from a landfill gas-fired power plant, Renew. Sustain. Energy Rev. 16 (4) (2012) 1779–1789.
[10] Green, D.W. and R.H. Perry, Perry's Chemical Engineers' Handbook. 8th ed. 2008: McGraw-Hill.
[11] Y. Guo, J. Hu, X. Liu, T. Sun, S. Zhao, S. Wang, Scalable solvent-free preparation of [Ni 3 (HCOO) 6] frameworks for highly efficient separation of CH 4 from N 2, Chem. Eng. J. 327 (2017) 564–572.
[12] M. Hasanuzzaman, N.A. Rahim, M. Hosenuzzaman, R. Saidur, I.M. Mahbubul, M. M. Rashid, Energy savings in the combustion based process heating in industrial sector, Renew. Sustain. Energy Rev. 16 (7) (2012) 4527–4536.
[13] G. Hu, Q. Zhao, L. Tao, P. Xiao, P.A. Webley, K.G. Li, Enrichment of low grade CH4 from N2/CH4 mixtures using vacuum swing adsorption with activated carbon, Chem. Eng. Sci. 229 (2021), 116152.
[14] G. Hu, Q. Zhao, M. Manning, L. Chen, L. Yu, E.F. May, K.G. Li, Pilot scale assessment of methane capture from low concentration sources to town gas specification by pressure vacuum swing adsorption (PVSA), Chem. Eng. J. 427 (2022), 130810.
[15] I. Karakurt, G. Aydin, K. Aydiner, Mine ventilation air methane as a sustainable energy source, Renew. Sustain. Energy Rev. 15 (2) (2011) 1042–1049.
[16] I. Karakurt, G. Aydin, K. Aydiner, Sources and mitigation of methane emissions by sectors: a critical review, Renew. Energy 39 (1) (2012) 40–48.
[17] J. Kim, A. Maiti, L.C. Lin, J.K. Stolaroff, B. Smit, R.D. Aines, New materials for methane capture from dilute and medium-concentration sources, Nat. Commun. 4 (1) (2013) 1694.
[18] T.A. Kuznetsova, P.E. Fomenkov, N.G Kryuchenkova, A.M. Tolmachev, et al., Thermodynamics of adsorption of light hydrocarbons on microporous active carbons at supercritical temperatures. Protection of metals and physical chemistry of surfaces 53 (3) (2017) 404–407.
[19] P. Li, F. Handan Tezel, Pure and binary adsorption of methane and nitrogen by silicalite, J. Chem. Eng. Data 54 (1) (2009) 8–15.
[20] Y.L. Li, Y.S. Liu, Impact of bed length on low-concentration coal mine methane enrichment by proportion pressure swing adsorption, Int. J. Coal Prep. Util. 33 (2) (2013) 72–89.
[21] Y.L. Li, Y.S. Liu, X. Yang, Proportion pressure swing adsorption for low concentration coal mine methane enrichment, Sep. Sci. Technol. 48 (8) (2013) 1201–1210.
[22] F. Liu, Q. Lin, C. Fu, M. Wang, M. Han, C. Huang, H. Pan, F. Liu, Alkaline KMnO4 solution pretreat hydrochar to prepare high ultra-micropore volume carbon for CH4 enrichment from low-concentration coalbed methane, Fuel 303 (2021), 121301.
[23] J. Liu, H. Shang, J. Yang, J. Wang, J. Li, S. Deng, Novel zeolite/carbon monolith adsorbents for efficient CH4/N2 separation, Chem. Eng. J. 426 (2021), 130163.
[24] P. Marín, S. Ordóñez, F.V. Díez, Procedures for heat recovery in the catalytic combustion of lean methane-air mixtures in a reverse flow reactor, Chem. Eng. J. 147 (2–3) (2009) 356–365.

[25] P. Marín, F.V. Díez, S. Ordóñez, A new method for controlling the ignition state of a regenerative combustor using a heat storage device, Appl. Energy 116 (2014) 322–332.
[26] P. Marín, F.V. Díez, S. Ordóñez, Reverse flow reactors as sustainable devices for performing exothermic reactions: applications and engineering aspects, Chem. Eng. Process. - Process. Intensif. 135 (2019) 175–189.
[27] P. Marín, Z. Yang, Y. Xia, S. Ordóñez, Concentration of unconventional methane resources using microporous membranes: process assessment and scale-up, J. Nat. Gas. Sci. Eng. 81 (2020), 103420.
[28] P. Marín, A. Vega, F.V. Díez, S. Ordóñez, Control of regenerative catalytic oxidizers used in coal mine ventilation air methane exploitation, Process Saf. Environ. Prot. 134 (2020) 333–342.
[29] J. McEwen, J.-D. Hayman, A. Ozgur Yazaydin, A comparative study of CO_2, CH4 and N2 adsorption in ZIF-8, Zeolite-13X and BPL activated carbon, Chem. Phys. 412 (2013) 72–76.
[30] I.E. Men'shchikov, A.A. Fomkin, A.Y. Tsivadze, A.V. Shkolin, E.M. Strizhenov, E. V. Khozina, Adsorption accumulation of natural gas based on microporous carbon adsorbents of different origin, Adsorption 23 (2) (2017) 327–339.
[31] G. Myhre, et al., Anthropogenic and Natural Radiative Forcing. Climate Change 2013: The physical science basis. Contribution of Working Group I to the Fifth Assessment Report of the Intergovernmental Panel on Climate Change, Cambridge University Press, Cambridge, 2013, pp. 659–740.
[32] R. Peláez, P. Marín, F.V. Díez, S. Ordóñez, Direct synthesis of dimethyl ether in multi-tubular fixed-bed reactors: 2D multi-scale modelling and optimum design, Fuel Process. Technol. 174 (2018) 149–157.
[33] Z. Qian, Y. Yang, P. Li, J. Wang, A.E. Rodrigues, An improved vacuum pressure swing adsorption process with the simulated moving bed operation mode for CH4/N2 separation to produce high-purity methane, Chem. Eng. J. 419 (2021), 129657.
[34] D. Qu, Y. Yang, Z. Qian, P. Li, J. Yu, A.M. Ribeiro, A.E. Rodrigues, Enrichment of low-grade methane gas from nitrogen mixture by VPSA with CO_2 displacement process: modeling and experiment, Chem. Eng. J. 380 (2020), 122509.
[35] X. Ren, T. Sun, J. Hu, S. Wang, Synthesis optimization of the ultra-microporous [Ni3(HCOO)6] framework to improve its CH4/N2separation selectivity, RSC Adv. 4 (80) (2014) 42326–42336.
[36] T.E. Rufford, G.C.Y. Watson, T.L. Saleman, P.S. Hofman, N.K. Jensen, E.F. May, Adsorption equilibria and kinetics of methane + nitrogen mixtures on the activated carbon norit RB3, Ind. Eng. Chem. Res. 52 (39) (2013) 14270–14281.
[37] S. Su, A. Beath, H. Guo, C. Mallett, An assessment of mine methane mitigation and utilisation technologies, Prog. Energy Combust. Sci. 31 (2) (2005) 123–170.
[38] D. Ursueguía, E. Díaz, S. Ordóñez, Metal-organic frameworks (MOFs) as methane adsorbents: from storage to diluted coal mining streams concentration, Sci. Total Environ. 790 (2021), 148211.
[39] D. Ursueguía, P. Marín, E. Díaz, S. Ordóñez, A new strategy for upgrading ventilation air methane emissions combining adsorption and combustion in a lean-gas turbine, J. Nat. Gas. Sci. Eng. 88 (2021), 103808.
[40] L.J.P. Van Den Broeke, R. Krishna, Experimental verification of the Maxwell-Stefan theory for micropore diffusion, Chem. Eng. Sci. 50 (16) (1995) 2507–2522.
[41] G.V.P. Varma, T. Srinivas, Power generation from low temperature heat recovery, Renew. Sustain. Energy Rev. 75 (2017) 402–414.
[42] S.-M. Wang, P.C. Wu, J.W. Fu, Q.Y. Yang, Heteroatom-doped porous carbon microspheres with ultramicropores for efficient CH4/N2 separation with ultra-high CH4 uptake, Sep. Purif. Technol. 274 (2021), 119121.
[43] G. Xiao, Z. Li, T.L. Saleman, E.F. May, Adsorption equilibria and kinetics of CH4 and N2 on commercial zeolites and carbons, Adsorption 23 (1) (2017) 131–147.
[44] X. Yang, Y. Liu, Z. Li, C. Zhang, Y. Xing, Vacuum exhaust process in pilot-scale vacuum pressure swing adsorption for coal mine ventilation air methane enrichment, Energies 11 (5) (2018) 1030.
[45] Y. Yang, A.M. Ribeiro, P. Li, J.G. Yu, A.E. Rodrigues, Adsorption equilibrium and kinetics of methane and nitrogen on carbon molecular sieve, Ind. Eng. Chem. Res. 53 (43) (2014) 16840–16850.
[46] A. Zagoruiko, Reverse-Flow. Oper. Catal. React.: Hist. Prospects 10 (2012) 113–129.